Chinese Journal of Aeronautics, (2023), **36**(3): 80–95

Chinese Society of Aeronautics and Astronautics
& Beihang University

Chinese Journal of Aeronautics

cja@buaa.edu.cn
www.sciencedirect.com

Hypersonic shock wave and turbulent boundary layer interaction in a sharp cone/flare model

Fulin TONG [a,b], **Junyi DUAN** [c,d], **Jiang LAI** [a,b], **Dong SUN** [a,b], **Xianxu YUAN** [a,b,*]

[a] *State Key Laboratory of Aerodynamics, China Aerodynamics Research and Development Center, Mianyang 621000, China*
[b] *Computational Aerodynamics Institute, China Aerodynamics Research and Development Center, Mianyang 621000, China*
[c] *LHD, Institute of Mechanics, Chinese Academy of Sciences, Beijing 100190, China*
[d] *School of Engineering Science, University of Chinese Academy of Sciences, Beijing 100049, China*

Received 10 January 2022; revised 20 February 2022; accepted 11 March 2022
Available online 25 July 2022

KEYWORDS

Shock wave;
Hypersonic turbulent boundary layer;
Heat transfer;
Skin friction decomposition;
Direct numerical simulation

Abstract A direct numerical simulation of hypersonic Shock wave and Turbulent Boundary Layer Interaction(STBLI) at Mach 6.0 on a sharp 7° half-angle circular cone/flare configuration at zero angle of attack is performed. The flare angle is 34° and the momentum thickness Reynolds number based on the incoming turbulent boundary layer on the sharp circular cone is $Re_\theta = 2506$. It is found that the mean flow is separated and the separation bubble occurring near the corner exhibits unsteadiness. The Reynolds analogy factor changes dramatically across the interaction, and varies between 1.06 and 1.27 in the downstream region, while the QP85 scaling factor has a nearly constant value of 0.5 across the interaction. The evolution of the reattached boundary layer is characterized in terms of the mean profiles, the Reynolds stress components, the anisotropy tensor and the turbulence kinetic energy. It is argued that the recovery is incomplete and the near-wall asymptotic behavior does not occur for the hypersonic interaction. In addition, mean skin friction decomposition in an axisymmetric turbulent boundary layer is carried out for the first time. Downstream of the interaction, the contributions of transverse curvature and body divergence are negligible, whereas the positive contribution associated with the turbulence kinetic energy production and the negative spatial-growth contribution are dominant. Based on scale decomposition, the positive contribution is further divided into terms with different spanwise length scales. The negative contribution is analyzed by comparing the convective term, the streamwise-heterogeneity term and the pressure gradient term.

* Corresponding author.
E-mail address: yuanxianxu@cardc.cn (X. YUAN).
Peer review under responsibility of Editorial Committee of CJA.

Production and hosting by Elsevier

1. Introduction

Understanding the physical phenomena associated with Shock wave and Turbulent Boundary Layer Interaction (STBLI) is of practical importance in the aeronautical and aerospace industries, because the shock-induced fluctuations of pressure and heat transfer are particularly severe, and are often responsible

https://doi.org/10.1016/j.cja.2022.07.023
1000-9361

for thermal and structural failure of high-speed aircraft. Comprehensive review articles on the interaction have been published by Green,[1] Dolling[2] and Gaitonde,[3] who extensively discuss the physics as well as the computational and experimental methods used to address the problem. Depending on the complexity of the interaction, Gaitonde[3] has divided the canonical configurations used in STBLI into seven categories: impinging shock, compression ramp, cylinder flare or double cone, swept ramp (or corner), single sharp fin, double fin and internal flow.

There exists a wide body of experiments and numerical investigations by means of Direct Numerical Simulation (DNS) and Large-Eddy Simulation (LES) in the published literature for the nominally two-dimensional configurations, impinging shocks and compression ramps. Significant advances in the fundamental physics of STBLIs have been made over the past few decades, in areas such as the source of low-frequency unsteadiness,[4–7] turbulence amplification[8,9] and Görtler-like vortices.[10,11] For example, as reviewed by Clemens and Narayanaswamy,[4] low-frequency unsteadiness in the interaction region is driven either by the fluctuations in the upstream Turbulent Boundary Layer (TBL) or by the intrinsic instability of the downstream separated flow, which is dependent on the size of the separated flow. They concluded that the downstream mechanism is mainly dominant for large flow separation, while the upstream and downstream mechanisms are both present in weakly separated flows. Fang et al.[9] reviewed the mechanism of turbulence amplification in STBLIs and suggested that turbulence amplification in the upstream part of the interaction zone is caused by the interaction between the deceleration of the mean flow and streamwise velocity fluctuations, rather than the free shear layer. Using Dynamic Mode Decomposition (DMD), Priebe et al.[10] found that the reconstructed flow using the five low-frequency DMD modes exhibited similarities with the counter-rotating Görtler-like vortices. Recently, the presence of Görtler-like vortices in impinging shock wave and turbulent boundary layer interactions was experimentally demonstrated for the first time by Zhuang et al.[11] They discussed the absence of these vortices in previous studies, and proposed a possible mechanism for their generation in the reflected interactions. Despite remarkable progress, the majority of previous research has focused on supersonic STBLIs, and a comprehensive understanding of hypersonic interactions requires further study.

Until now, due to the difficulty of reliable and accurate turbulence measurements at high Mach number, there have been very limited experimental studies of hypersonic STBLIs including both mean and statistical turbulence quantities. An example is the particularly important measurement of turbulence fluctuations across the interaction region taken in the early experiment by Mikulla and Horstman[12] for two Mach 7 axisymmetric reflected interactions. Comparison of the separated and attached flows showed that a coupling between turbulent energy and separation bubble unsteadiness was responsible for substantial differences in turbulence lifetimes. Later, similar experiments were performed at Mach 8 by Bookey et al.[13] on an 8° compression corner, at Mach 7 by Schrijer et al.[14] on a double ramp flow and, more recently, at Mach 10 by Brooks et al.[15] on a hollow cylinder flare. These experiments demonstrate a strong amplification throughout the interaction. The recent particle image velocimetry data acquired by Schreyer et al.[16] at Mach 7.2 for 8° and 33° compression corners show a different amplification process for the fluctuation components, where the peak locations are further moved away from the wall in the strong interaction.

Recently, a preliminary attempt to perform a DNS analysis of hypersonic STBLI was carried out by Priebe and Martin,[17] who analyzed the evolution of turbulence on an 8° compression ramp at $Ma_\infty = 7.2$ and $Re_\theta = 3500$. In their attached STBLI, the Reynolds stress components were found to be amplified by factors of 1.8–2.5, and the turbulence became more isotropic in the interaction region. A quantitative analysis of the heat transfer showed that the commonly used Reynolds analogy did not apply in the interaction, and the heat transfer scaled better with pressure, rather than skin friction.

The objective of this paper is to systematically investigate hypersonic STBLI on a sharp cone/flare by means of DNS. To the best of the authors' knowledge, no other DNS studies of hypersonic interactions on the axisymmetric configuration have been reported so far. The geometry and the inflow conditions model used in the present study closely approximate recent experiments on a 7° half-angle circular cone/flare in the Air Force Research Laboratory (AFRL) Mach-6 Ludwieg tube by Running et al.[18] The flare angle is set to 34° and the mean flow in the interaction is separated. In this study, we comprehensively analyze the recovery of the reattached boundary layer and the generation of mean skin friction and heat transfer in the downstream region.

2. Numerical methodology

2.1. Governing equations

We use a high-order finite-difference DNS code, OpenCFD-SC, to solve the three-dimensional compressible conservative Navier-Stokes equations in conical coordinates without any modeling. This code has been extensively validated for supersonic and hypersonic flows including STBLIs over a compression ramp[19] and incident shock interaction over a wavy-wall.[20] In this study, the governing equations are non-dimensionalized by the inflow parameters and the reference length scale (in millimeters), and are written as

$$\frac{\partial \boldsymbol{U}}{\partial t}+\frac{\partial(\boldsymbol{E}-\boldsymbol{E}_{\mathrm{v}})}{\partial z}+\frac{\partial(\boldsymbol{F}-\boldsymbol{F}_{\mathrm{v}})}{\partial r}+\frac{\partial(\boldsymbol{G}-\boldsymbol{G}_{\mathrm{v}})}{\partial \varphi}=\boldsymbol{H} \tag{1}$$

where z, r and φ specify the axial, radial and azimuthal directions, respectively. The conservative vector flux is $\boldsymbol{U} = r[\rho\ \rho u\ \rho v\ \rho w\ \rho E_{\mathrm{t}}]^{\mathrm{T}}$, with ρ, u, v, w and E_{t} being the density, the components of velocity in the directions z, r and φ, and the total energy, respectively. The inviscid terms ($\boldsymbol{E}$, $\boldsymbol{F}$, $\boldsymbol{G}$), the viscous terms ($\boldsymbol{E}_{\mathrm{v}}$, $\boldsymbol{F}_{\mathrm{v}}$, $\boldsymbol{G}_{\mathrm{v}}$) and the source term $\boldsymbol{H}$ are given by.

$$\boldsymbol{E}=r\begin{bmatrix}\rho u\\ \rho u^2+p\\ \rho uv\\ \rho uw\\ u(\rho E_{\mathrm{t}}+p)\end{bmatrix},\boldsymbol{F}=r\begin{bmatrix}\rho v\\ \rho vu\\ \rho v^2+p\\ \rho vw\\ v(\rho E_{\mathrm{t}}+p)\end{bmatrix},\boldsymbol{G}=\begin{bmatrix}\rho w\\ \rho wu\\ \rho wv\\ \rho w^2+p\\ w(\rho E_{\mathrm{t}}+p)\end{bmatrix}$$

$$\boldsymbol{E}_{\mathrm{v}}=r\begin{bmatrix}0\\ \sigma_{11}\\ \sigma_{21}\\ \sigma_{31}\\ u\sigma_{11}+v\sigma_{21}+w\sigma_{31}-\frac{\mu}{(\gamma-1)Re_\infty PrMa_\infty^2}\cdot\frac{\partial T}{\partial z}\end{bmatrix}$$

$$\boldsymbol{F}_{\mathrm{v}} = r\begin{bmatrix} 0 \\ \sigma_{12} \\ \sigma_{22} \\ \sigma_{32} \\ u\sigma_{12} + v\sigma_{22} + w\sigma_{32} - \frac{\mu}{(\gamma-1)Re_\infty PrMa_\infty^2}\cdot\frac{\partial T}{\partial r} \end{bmatrix}$$

$$\boldsymbol{G}_{\mathrm{v}} = \begin{bmatrix} 0 \\ \sigma_{13} \\ \sigma_{23} \\ \sigma_{33} \\ u\sigma_{13} + v\sigma_{23} + w\sigma_{33} - \frac{\mu}{(\gamma-1)Re_\infty PrMa_\infty^2}\cdot\frac{\partial T}{r\partial\varphi} \end{bmatrix}$$

$$\boldsymbol{H} = \begin{bmatrix} 0 \\ 0 \\ \rho w^2 + p - \sigma_{33} \\ -\rho vw + \sigma_{23} \\ 0 \end{bmatrix} \tag{2}$$

Here, $Re_\infty = v_\infty U_\infty L$ is the Reynolds number based on the inflow kinetic viscosity v_∞, the inflow freestream velocity U_∞ and the reference length scale L. The thermodynamic pressure p and the temperature T are assumed to obey the non-dimensionalized ideal gas state equation,$p = \rho T/\left(\gamma Ma_\infty^2\right)$. The Prandtl number and the specific heat capacity ratio are set to $Pr = 0.72$ and $\gamma = 1.4$, respectively. The viscous stresses are computed as

$$\begin{cases} \sigma_{11} = 2\frac{\mu}{Re_\infty}\left(\frac{\partial u}{\partial x} - \frac{1}{3}\mathrm{div}\boldsymbol{V}\right) \\ \sigma_{22} = 2\frac{\mu}{Re_\infty}\left(\frac{\partial v}{\partial r} - \frac{1}{3}\mathrm{div}\boldsymbol{V}\right) \\ \sigma_{33} = 2\frac{\mu}{Re_\infty}\left(\frac{1}{r}\cdot\frac{\partial w}{\partial\varphi} + \frac{v}{r} - \frac{1}{3}\mathrm{div}\boldsymbol{V}\right) \\ \sigma_{12} = \frac{\mu}{Re_\infty}\left(\frac{\partial v}{\partial x} + \frac{\partial u}{\partial r}\right) \\ \sigma_{13} = \frac{\mu}{Re_\infty}\left(\frac{\partial w}{\partial x} + \frac{1}{r}\cdot\frac{\partial u}{\partial\varphi}\right) \\ \sigma_{23} = \frac{\mu}{Re_\infty}\left(\frac{1}{r}\cdot\frac{\partial v}{\partial\varphi} + \frac{\partial w}{\partial r} - \frac{w}{r}\right) \end{cases} \tag{3}$$

where $\mathrm{div}\boldsymbol{V}$ represents the divergence of velocity in the conical coordinate system. The molecular viscosity μ is determined by Sutherland's law, given as

$$\mu = T^{3/2}\frac{(1 + T_{\mathrm{s}}/T_\infty)}{(T + T_{\mathrm{s}}/T_\infty)} \tag{4}$$

with T_∞ being the inflow static temperature and $T_{\mathrm{s}} = 110.4$ K. Unless otherwise stated, the subscript"∞" stands for a variable in the inflow freestream.

2.2. Numerical scheme

In the DNS code, the inviscid terms are calculated using the WENO-SYMBO scheme[21] with limiters[22] and the Steger-Warming vector flux splitting method. WENO-SYMBO is a bandwidth-optimized, 4th-order Weighted Essentially Non-Oscillatory (WENO) scheme that uses a symmetric collection of candidate stencils in the linear part of the original WENO method. Employing an absolute limiter in the smoothness measurement and a relative limiter based on the total variation, together, to further reduce numerical dissipation and to stabilize the simulation, WENO-SYMBO can properly resolve turbulence in the smooth region, while shock waves are still well captured. The viscous terms are discretized by an 8th-order central difference scheme, and the 3rd-order Runge-Kutta method[23] is used to perform the time integration.

2.3. Computation overview

Fig. 1 shows the sharp cone/flare model used in the present simulation, which closely approximates the recent experiments conducted in the AFRL Ludwieg tube by Running et al.[18] An instantaneous iso-surface of density gradient colored by wall-normal distance is included. In Fig. 1, the variable z_{o} is the location of the domain inlet, z_{a} and z_{b} denote the start and end points of the blowing and suction region, z_{ref} is the reference location in the upstream fully developed TBL. The sharp circular cone has a length of 609 mm and a half vertex angle of 7°, followed by the 34° flare with a length of 76 mm. The approach flow has a Mach number of $Ma_\infty = 6.0$, a unit inflow Reynolds number of $Re_\infty = 10.8 \times 10^3$ /mm and a static temperature of $T_\infty = 65$ K. Following the DNS by Li et al.[20] and Sivasubramanian and Fasel,[24] the computational domain (see Fig. 1) does not include the tip of the cone, which ranges from $z = 156$ mm to $z = 675$ mm. The domain height in the wall-normal direction is set to be 40 mm, and the domain size in the azimuthal direction corresponds to a span of $\varphi = 11.5°$. Similar to the laminar-to-turbulent transition method of Pirozzoli et al.,[25] a region of strong random blowing and suction disturbances is enforced along the wall ranging from $z = 180$ mm to $z = 185$ mm. As a result, the inflow laminar boundary layer is triggered, and fully turbulent conditions are produced at the reference location $z_{\mathrm{ref}} = 580$ mm, just upstream of the 34° flare. At z_{ref}, the boundary layer thickness is estimated to be $\delta = 5.88$ mm and the friction Reynolds number and the momentum thickness *R*eynolds number are $Re_\tau = 343$ and $Re_\theta = 2506$, respectively.

The computation grid and boundary conditions are illustrated in Fig. 2. The grid is plotted at intervals of every ten and five points in the x and y directions, respectively. Unless otherwise specified, x and y denote the streamwise direction along the wall and the wall-normal direction, respectively, with u_{s} and u_{n} the corresponding velocity components. In the x direction, a total number of 4819 points is used to discretize the domain, which is bounded by a laminar boundary layer at the domain inlet and a supersonic outflow boundary at the domain outlet. Specifically, 2820 points are equally distributed in the interaction region 576 mm $< z <$ 660 mm, corresponding to a grid resolution of $\Delta x^+ = 2.72$ in terms of the wall units taken at z_{ref}. There are 1950 points distributed with gradually increasing separation in the transition region 156 mm $< z <$ 576 mm. In the buffer region $z >$ 660 mm, 49 points are located with progressively coarsening grid spacing to inhibit the reflection of disturbances. In the following analysis, the superscript "+" refers to normalization with local wall units taken at z_{ref}. The profile of the imposed laminar boundary layer is determined from an auxiliary DNS of the sharp cone under the same inflow conditions. In the y direction, 319 points are clustered toward the wall, ensuring that there are 190 points located inside the boundary layer. Thus, the grid resolutions at the first point from the wall and at the edge of the boundary layer are $\Delta y^+ = 0.59$ and $\Delta y^+ = 4.24$, respectively, comparable with those in recent DNS

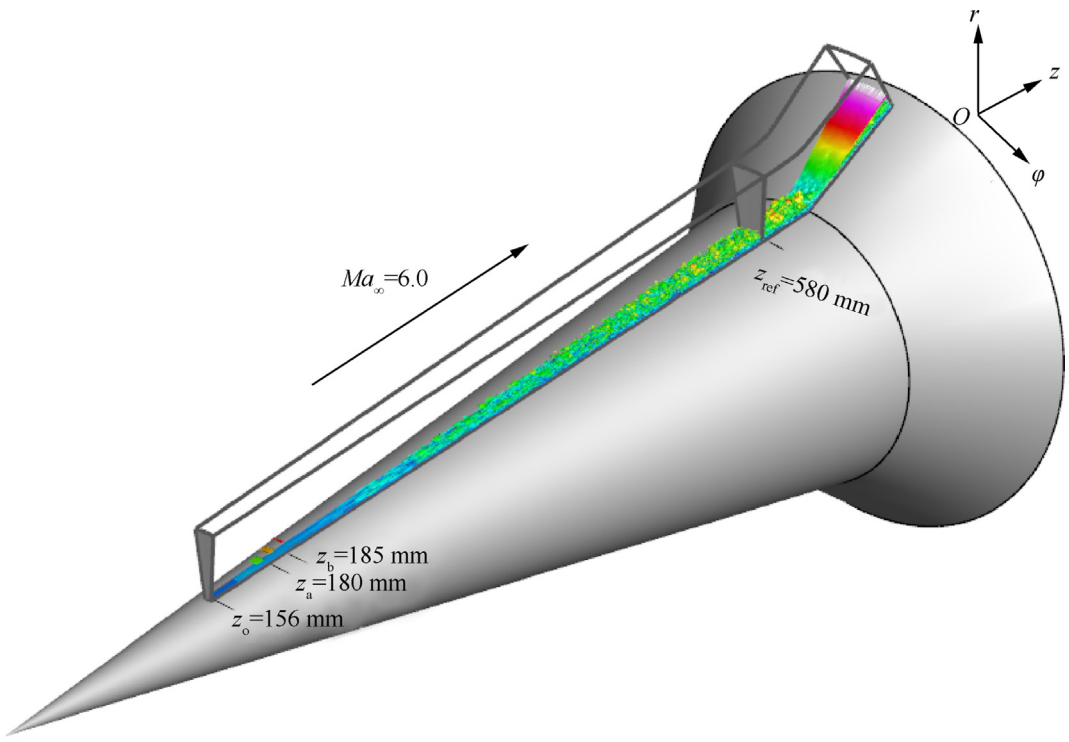

Fig. 1 Sketch of sharp cone/flare model and computational domain.

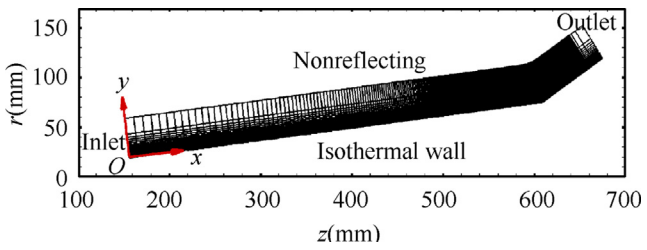

Fig. 2 A two-dimensional sketch of computational grid and boundary conditions.

studies on a hypersonic compression ramp flow by Priebe and Martin.[17] At the bottom boundary, the wall is modeled with no-slip isothermal boundary conditions, and the wall temperature is set to be $T_w = 296$ K, corresponding to a cold wall with wall-to-recovery temperature ratio $T_w/T_r = 0.62$. The velocity disturbances in the wall blowing and suction region (see Fig. 1, $z_a < z < z_b$) are similar to those in previous simulations by Li et al.,[20,26] where random numbers between $-\beta$ and β are spatially randomly distributed and kept temporally constant. In order to greatly accelerate the transition process over the sharp cone, we choose $\beta = 0.4$, much larger than the value used by Li et al.[20] In addition, as suggested by Pirozzoli et al.,[27] nonreflecting boundary conditions are used at the upper boundary to inhibit the reflection of spurious disturbances. In the φ direction, periodic boundary conditions are enforced due to the homogeneity in the azimuthal direction, with 360 points being equally distributed. The grid spacing increases from $\Delta r\varphi^+ = 2.31$ at z_{ref} to $\Delta r\varphi^+ = 3.55$ at $z = 660$ mm, caused by the rapid increase of the radius of the 34° flare angle.

We performed a sensitivity study to assess the chosen grid resolution and the domain extent in the azimuthal direction. The selected mesh ($N_x \times N_y \times N_\varphi = 4819 \times 319 \times 360$) is labeled as Grid-B, and another three grids are labeled as Grid-A, Grid-C and Grid-D. Grid-A is generated by coarsening 30% of the grid spacing in both the x and φ directions, corresponding to $N_x \times N_y \times N_\varphi = 3917 \times 319 \times 240$. In contrast, from Grid-B to Grid-C, the grid is refined by 30% in both the x and φ directions, so $N_x \times N_y \times N_\varphi = 5719 \times 319 \times 480$. For Grid-D, the azimuthal domain extent only is increased by 50%, so $N_x \times N_y \times N_\varphi = 4819 \times 319 \times 540$. Note that the variation of the grid resolution in the x direction is applied in the interaction region, whereas the grid resolutions in the transition region and the buffer region are not changed. Fig. 3 shows a comparison of mean wall quantities for Grid-A to Grid-D. In the results that follow, the mean refers to the average in time and in the azimuthal direction. It is clear that the curves for mean wall pressure p_w (see Fig. 3(a)) agree very well, and the streamwise locations of mean separation and reattachment point are insensitive to the variations of grid resolution and domain size (see Fig. 3(c)). Slight variations are found only in the mean skin fiction coefficient C_f and heat transfer coefficient C_h on the flare $z > 620$ mm. The results with Grid-A exhibit a deviation of approximately 10% from those with Grid-B, while the relative differences between the other three grids are confined within 5%, indicating that Grid-B is sufficient to obtain converged results and the selected azimuthal domain size is reasonable.

The adequacy of the adopted azimuthal domain extent is further assessed by analyzing the two-point autocorrelation function in the φ direction, which is defined as[25,27]

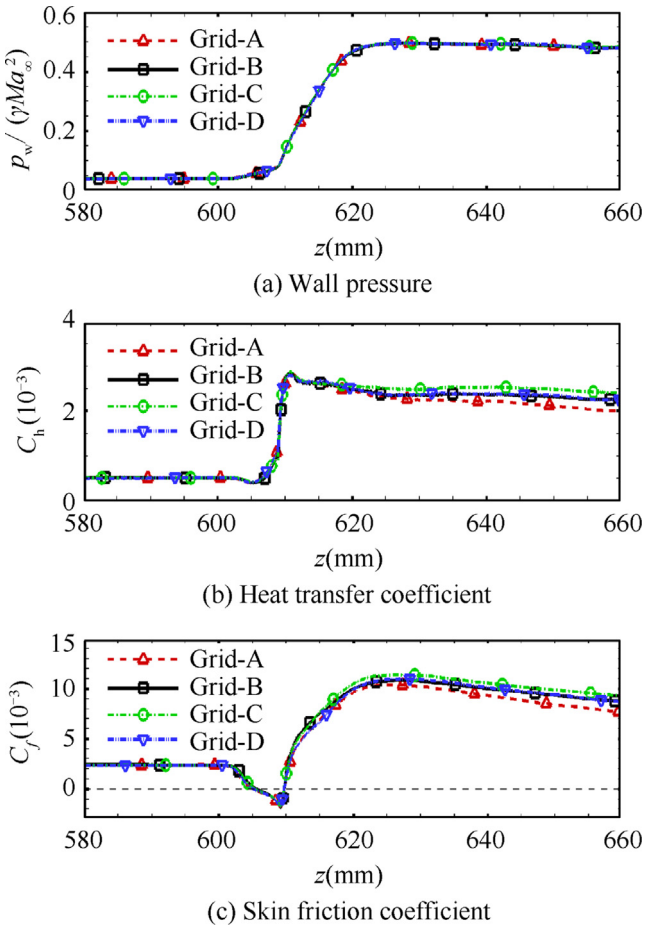

Fig. 3 Grid and domain sensitivity study with respect to mean wall quantities evolution.

$$R_{\alpha\alpha}(s_\varphi) = \frac{\overline{\alpha(x,y,s)\alpha(x,y,s+s_\varphi)}}{\overline{\alpha^2(x,y,s)}^{1/2}\overline{\alpha^2(x,y,s+s_\varphi)}^{1/2}} \quad (5)$$

in which the bar denoting averages in time and in the φ direction, and s_φ and s representing the spacing and the coordinate in the azimuthal direction, respectively. Fig. 4 shows the two-point autocorrelations for the fluctuations of density, temperature and velocity components at two wall-normal locations in the interaction region, where $y^+ = 6.7$ and $y^+ = 85$ at $z = 617$ mm. Both figures show that all the correlations decay rapidly and the fluctuations are decorrelated as the spacing is increased over half of the azimuthal width $L_\varphi/2$, confirming that the azimuthal domain used in the present simulation is wide enough and the turbulence fluctuations are not inhibited.

The simulation with Grid-B was carried out on a parallel cluster using 9600 cores and a total budget of 3.2×10^6 CPU hours. After a washout time of two flow-through times (i.e., $2L_z/U_\infty$, L_z being the domain length in the z direction), the simulation is performed for four flow-through times once the flow in the interaction region had reached a statistically stationary state. A total of 400 samples of the three-dimensional flow field were collected at a constant time interval to guarantee statistical convergence. The flow statistics detailed below are obtained using averages in time and in the φ direction. As an aside, fully time-resolved samples in the

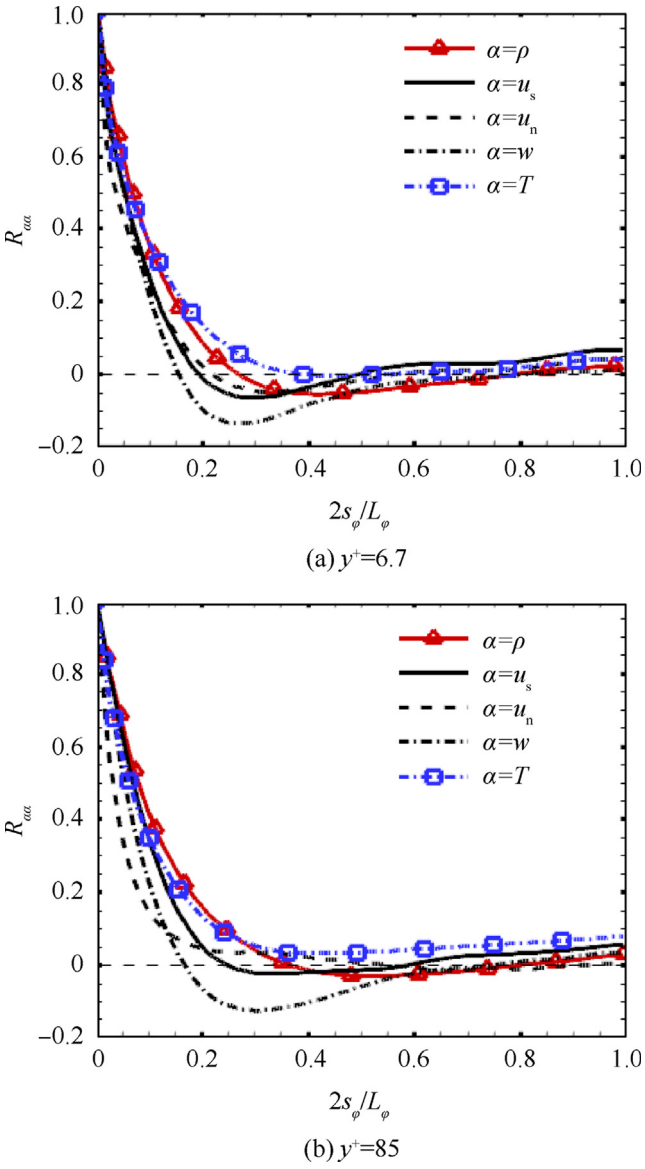

Fig. 4 Distributions of two-point autocorrelation coefficient at different wall-normal locations in the interaction region $z = 617$ mm.

z-r plane at $\varphi = 5.75°$ were also gathered for the time-varying analysis below, and 4300 samples at five selected streamwise locations were collected at short time intervals to obtain accurate estimates of energy spectra in the decomposition analysis. For a generic variable ϕ, the Reynolds average and the Favre average are defined as $f = \bar{f} + f'$ and $f = \tilde{f} + f''$, where $\tilde{f} = \overline{\rho f}/\bar{f}$, f' and f'' being the corresponding fluctuations.

3. Results and discussion

3.1. Upstream turbulent boundary layer

An instantaneous numerical schlieren visualization of the upstream TBL is shown in Fig. 5, with the domain rotated 7° clockwise. The variable, defined as $d_s = 0.8\exp[-10(|\nabla$

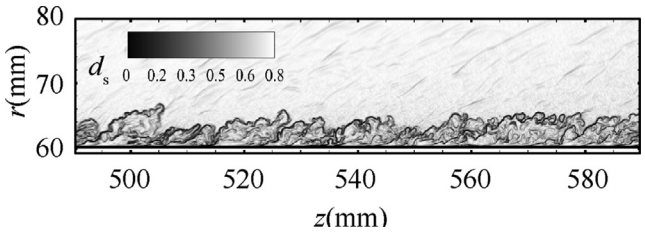

Fig. 5 Instantaneous numerical schlieren visualization of upstream TBL.

$\rho|-|\nabla\rho|_{\min})/(|\nabla\rho|_{\max}-|\nabla\rho|_{\min})]$, is a nonlinear function of the magnitude of the density gradient $|\nabla\rho|$, often used in previous DNS studies of STBLIs.[17,28] With this transformation, the dark regions in the figure denote large density gradients in the flow field; the visualization exhibits a pattern consistent with observations in previous experiments. As observed by Prebie and Martin[17] in a DNS of a Mach 7.2 turbulent boundary layer and by Bookey et al.[13] in experiments on Mach 8 flows, sharp interfaces are clearly observed at the boundary layer edge, which separates the turbulent structures from the outer irrotational fluid, and the inclined turbulent bulges with high intermittency are highlighted inside the boundary layer.

Fig. 6 shows a quantitative comparison of turbulence statistics taken at the reference location z_{ref} with previous experimental and numerical results. In Fig. 6(a), the van Direst transformed mean streamwise velocity U_{vd}^{+} profile agrees very well with the DNS data obtained by Priebe and Martin[17] at $Re_\theta = 3350$, except for notable differences in the wake region due to the different Reynolds number used. The classic law of the wall is only satisfied in the region $y^+ < 5$, and a narrow logarithmic region is observed for $40 < y^+ < 80$, where the von Karman and log law constants are set to 0.41 and 5.8, respectively. Fig. 6(b) compares the profiles of the density-scaled Reynolds stress components R_{ij} with previous compressible DNS data at similar Reynolds numbers. In Fig. 6(b), u_τ is the friction velocity; δ is the reference boundary layer thickness. A satisfactory agreement with the numerical results reported by Pirozzoli et al.[29] in a spatially developing boundary layer at Mach 2 and $Re_\tau = 278$–358, and by Subbareddy and Candler[30] in a Mach 6 cold-wall boundary layer flow at $Re_\theta \approx 6000$, is obtained, confirming that the generation method of the incoming turbulent boundary layer used in the present study is reliable.

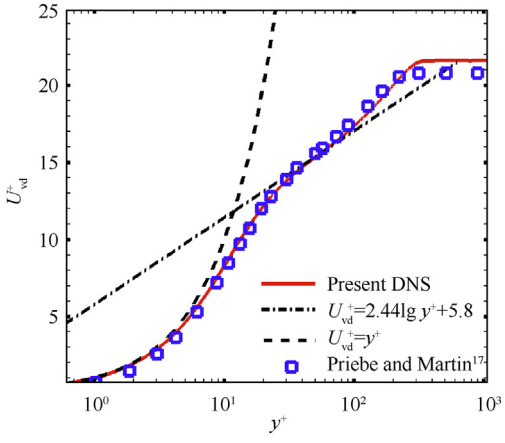

(a) Mean velocity profile

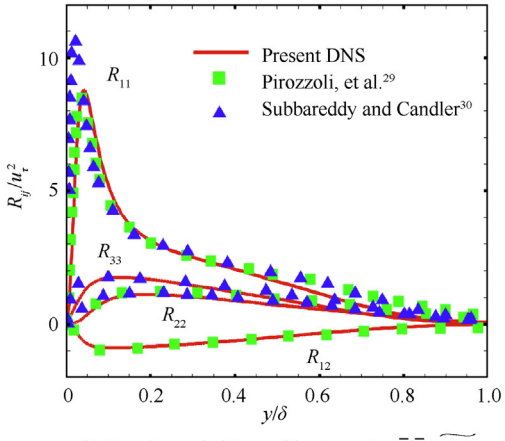

(b) Density-scaled Reynolds stress $R_{ij}=(\bar{\rho}/\bar{\rho}_w)\widetilde{u_i''u_j''}$

Fig. 6 Turbulence statistics obtained at the reference location z_{ref}.

3.2. Instantaneous and mean flow fields

To give a qualitative overview of the interaction region, Fig. 7 and Fig. 8 show contours of instantaneous density gradient and mean pressure, respectively. In Fig. 7, the foot of the strong shock penetrates into the boundary layer, and the thickness of the disturbed boundary layer decreases significantly, with a slow increase in the recovery region. Downstream of the interaction, the pressure is strongly amplified and the density gradient becomes much steeper (as reflected by the darker region at $z > 610$ mm), due to the strong adverse pressure gradient caused by the large deflection angle and the high inflow Mach number. As is observed in Fig. 8, a small region of separation bubble occurs at 605 mm $< z <$ 610 mm.

Computed instantaneous streamwise velocity fields in the z-r mid-plane are shown in Fig. 9, which shows two uncorrelated samples of the DNS flow field. The pink dash-dot line shows where the streamwise velocity $u = 0$, and the mean separation and reattachment points are denoted by symbols S and R, respectively. It is seen from Fig. 9(a) that the separation bubble becomes much larger than the mean separation region, with significant reversed flows observed downstream of the reat-

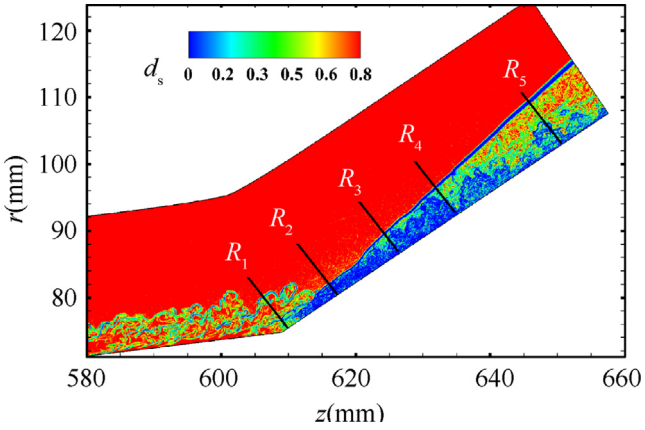

Fig. 7 Contours of instantaneous density gradient with five selected streamwise locations labeld as R_1-R_5.

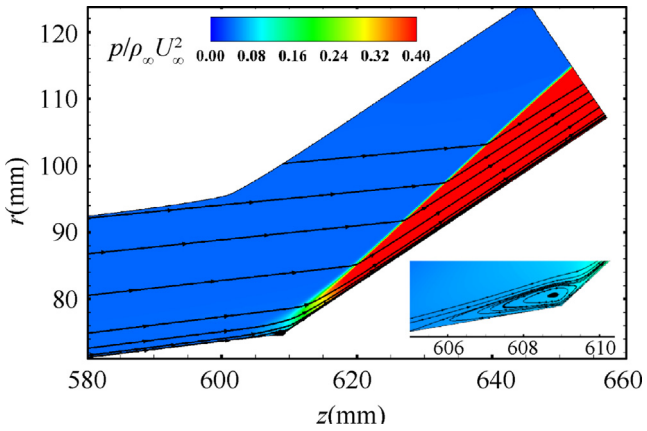

Fig. 8 Contours of mean pressure superimposed with in-plane streamlines(Inset is the enlargement of the separation region).

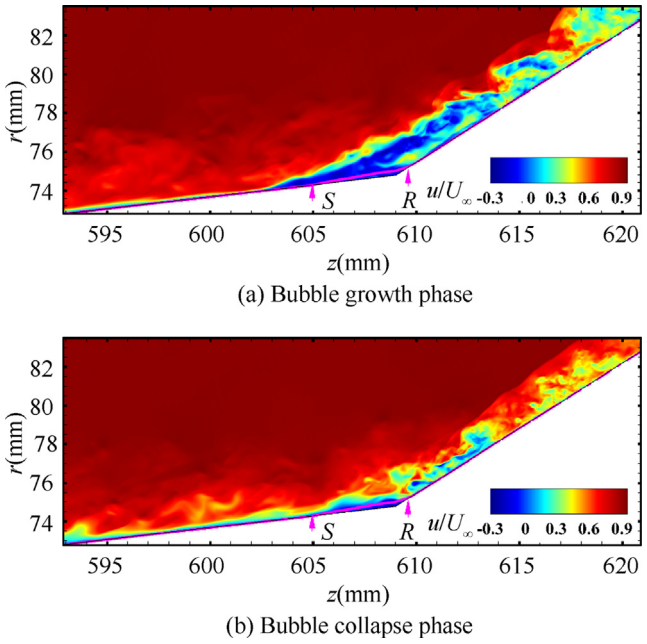

Fig. 9 Contours of two instantaneous streamwise velocity fields in the z-r mid-plane with mean streamwise velocity $u = 0$ isoline in pink.

tachment point, whereas the bubble in Fig. 9(b) is very small, with only a few locations with reversed flow concentrated below the mean separation region. This demonstrates the unsteady motion of the separated flow. Moreover, the variation in instantaneous bubble size (not shown here) reveals a breathing motion of the separation bubble, as previously observed by Priebe and Martin[31] in their DNS studies of a 24° compression ramp in Mach 2.9 flow.

To characterize the relation between mean wall quantities across the interaction zone, we analyze the distributions of the Reynolds analogy[32] and the QP85 scaling[33] factors, respectively. Here, the Reynolds analogy factor is defined as RAF $= 2C_h/C_f \approx 1$, and the QP85 scaling factor is defined as QP85 $= (C_h/C_{hu})\times(p_{wu}/p_w)^{0.85} \approx 1$, where p_{wu} and C_{hu} are the mean wall pressure and heat transfer coefficient, respectively, at z_{ref}. The Reynolds analogy distribution is shown in Fig. 10(a) as a function of z. Upstream of the interaction, RAF attains a nearly constant value of 1.07, agreeing well with what was previously shown by Roy and Blottner,[32] who found RAF = 0.9–1.3 in hypersonic zero-pressure-gradient boundary layers. In the separation region, RAF varies significantly and the Reynolds analogy is not satisfied, as a consequence of the small negative C_f. Past the reattachment point ($z > 610$ mm), RAF rapidly decreases, attaining a minimum value of RAF = 1.06 at $z = 628$ mm. Subsequently, it follows a slight increase in the recovery region, with RAF = 1.27 at $z = 660$ mm. In Fig. 10(b), it is seen that QP85 is nearly constant in the upstream TBL, where QP85 $\approx$ 1.0, consistent with the experimental results of Murray et al.,[34] whereas the QP85 scaling is not valid in the separation region, with QP85 varying between 0.6 and 1.8. However, it is worth noting that QP85 relaxes towards a nearly constant value (QP85 $\approx$ 0.5) in the recovery region at $z > 625$ mm, unlike in the DNS results of Priebe and Martin,[17] who found that QP85 monotonously decreased downstream of the interaction in a hypersonic compression ramp flow. This discrepancy is mainly ascribed to the different distribution of mean wall pressure. In our simulation, p_w is nearly constant in the downstream region, while the results of Priebe and Martin[17] exhibited a continuous increase.

3.3. Evolution of boundary layer

To obtain a better understanding of the recovery of the reattached boundary layer, we further compare turbulence statistics in terms of mean velocity and temperature profiles, Reynolds stress tensor components, anisotropy invariant maps and Turbulent Kinetic Energy (TKE), at five selected streamwise locations on the flare, denoted by R_1–R_5 as shown in Fig. 7. The first location R_1 is at the mean reattachment point $z = 610$ mm, while R_2–R_5 are located at $z = 617$ mm, 626 mm, 635 mm and 650 mm, respectively. In the following analysis, the reference boundary layer thickness δ is taken at z_{ref} for direct comparison.

Fig. 11(a) compares the mean streamwise velocity profiles at the five selected locations in the reattached boundary layer with that at z_{ref} in the upstream boundary layer, providing a general view of the recovery of the velocity profiles downstream of the interaction. It is seen that the upstream velocity profile is in good agreement with the DNS data of Priebe and Martin[17] at Mach 7.2 flow, characterized by typical TBL behavior. At R_1, very close to the reattachment point, the velocity significantly decreases for $y/\delta < 0.5$, and the profile becomes much less full, compared to that of z_{ref}. For R_2–R_5, we observe that only the velocities in the small inner region are fully recovered, whereas most parts of the downstream profiles strongly deviate from the upstream profile for $y/\delta > 0.1$. For instance, the velocities at $y/\delta = 0.1$ and 0.3 are about $0.60U_\infty$ and $0.63U_\infty$, respectively, for R_5, which are much lower than $0.72U_\infty$ and $0.84U_\infty$ for z_{ref}. It is suggested that the recovery process of the reattached boundary layer on the flare is not fully completed. Note that as the wall-normal location moves further away from the wall (above the shock wave), the velocities at R_3–R_5 sharply increase, finally approaching the freestream value. The corresponding temperature profiles are shown in Fig. 11(b), where the DNS data at z_{ref} and R_5 from the present study are compared with

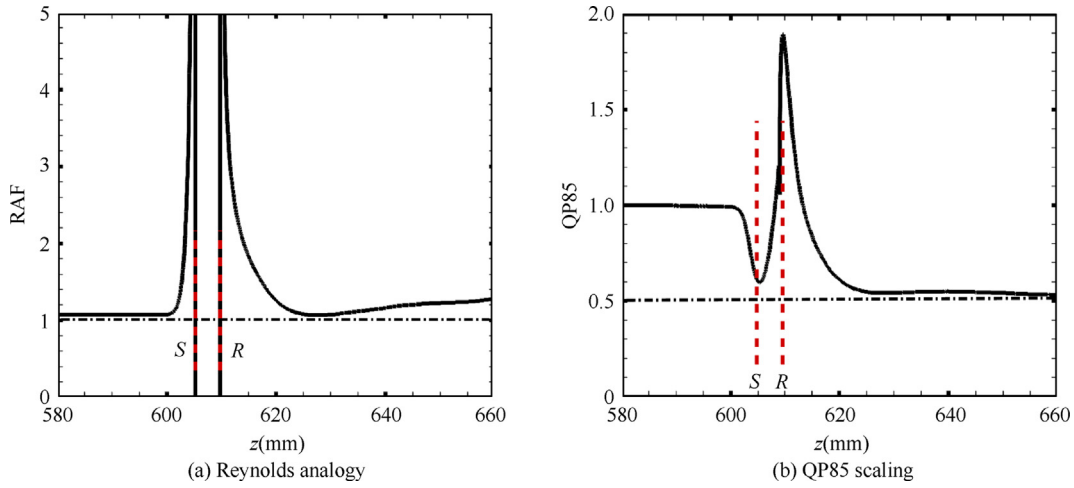

Fig. 10 Distribution of mean wall quantities.

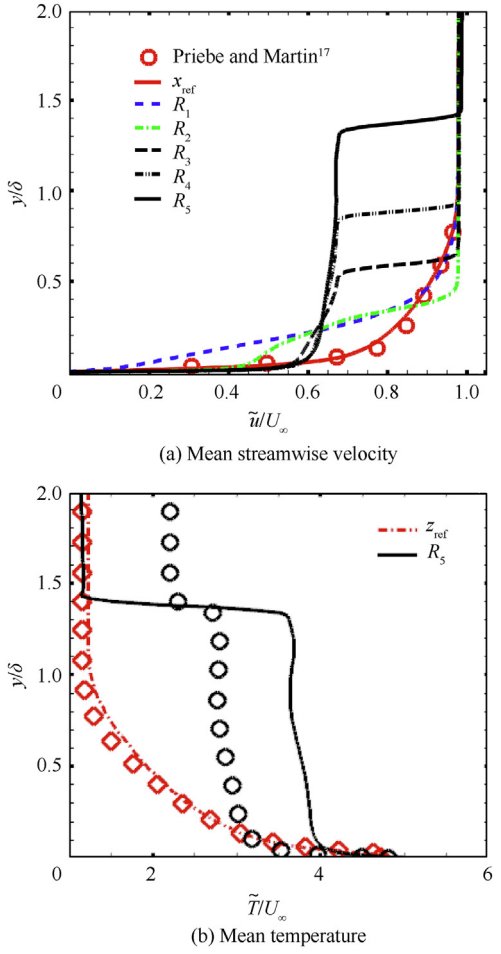

Fig. 11 Profiles of mean streamwise velocity and mean temperature at various streamwise locations.

predicted values obtained from the modified Crocco-Busemann relation given by Walz.[35] According to the modified Croco-Busemann relation, symbols in Fig. 11(b) represent the predicted temperatures at locations z_{ref} and R_5, respectively. As previously observed in supersonic turbulent boundary layers by Volpiani et al.[36] and Pirozzoli et al.,[27] the computed data at z_{ref} matches well the theoretical relation, indicating its reliability in characterizing the temperature–velocity relationship in hypersonic flows. We observe that the theoretical relation is not equally valid downstream of the interaction at R_5, where significant deviations are clearly observed and the predicted values are much smaller than the DNS data over most of the boundary layer.

The profiles of the Reynolds stress components at R_1-R_5 are plotted in Fig. 12. The results at z_{ref} are also included for comparison. As previously observed by Fang et al.[9] in a Mach 2.25 reflected interaction and by Loginov et al.[37] in compression ramp interactions, the figure highlights the large amplification of the Reynolds stress components downstream of the interaction. In particular, the components $\widetilde{u''u''}$, $\widetilde{v''v''}$, $\widetilde{w''w''}$ and $-\widetilde{u''v''}$ at R_1 are amplified by factors of about 3.0, 16.0, 9.0 and 17.0, respectively, consistent with the PIV measurements of two hypersonic STBLIs by Schreyer et al.,[16] who found that the wall-normal fluctuations were more strongly amplified than the streamwise component. At R_2–R_5, all components follow a continuous decrease as the reattached boundary layer develops downstream. Note that the strong spikes in Fig. 12 (b) and (d) are the direct result of the shock wave, which is located far away from the boundary layer edge, see Fig. 7. Importantly, we observe that the recovery of the streamwise component is much slower than those of the other three components. In Fig. 12(a), from z_{ref} to R_1, the peak of $\widetilde{u''u''}$ moves outwards and appears at $y/\delta \approx 0.1$, as often observed previously in separated STBLIs. This behavior is presumably related to the reattachment of the detached shear layer developing above the separation bubble in the interaction zone. From R_1 to R_2, the peak is shifted toward the wall instead, appearing in the very-near-wall region $y/\delta < 0.01$; this can be ascribed to the decay of the reattached shear layer and the regeneration of the near-wall structures. From R_3 to R_5, the magnitude gradually decreases, with the peak location changing slightly. It is seen that the profile at R_5 still significantly deviates from that of the upstream TBL, indicating that the recovery of the streamwise component is far from complete. Clearly, a different behavior is observed in Fig. 12(b)-

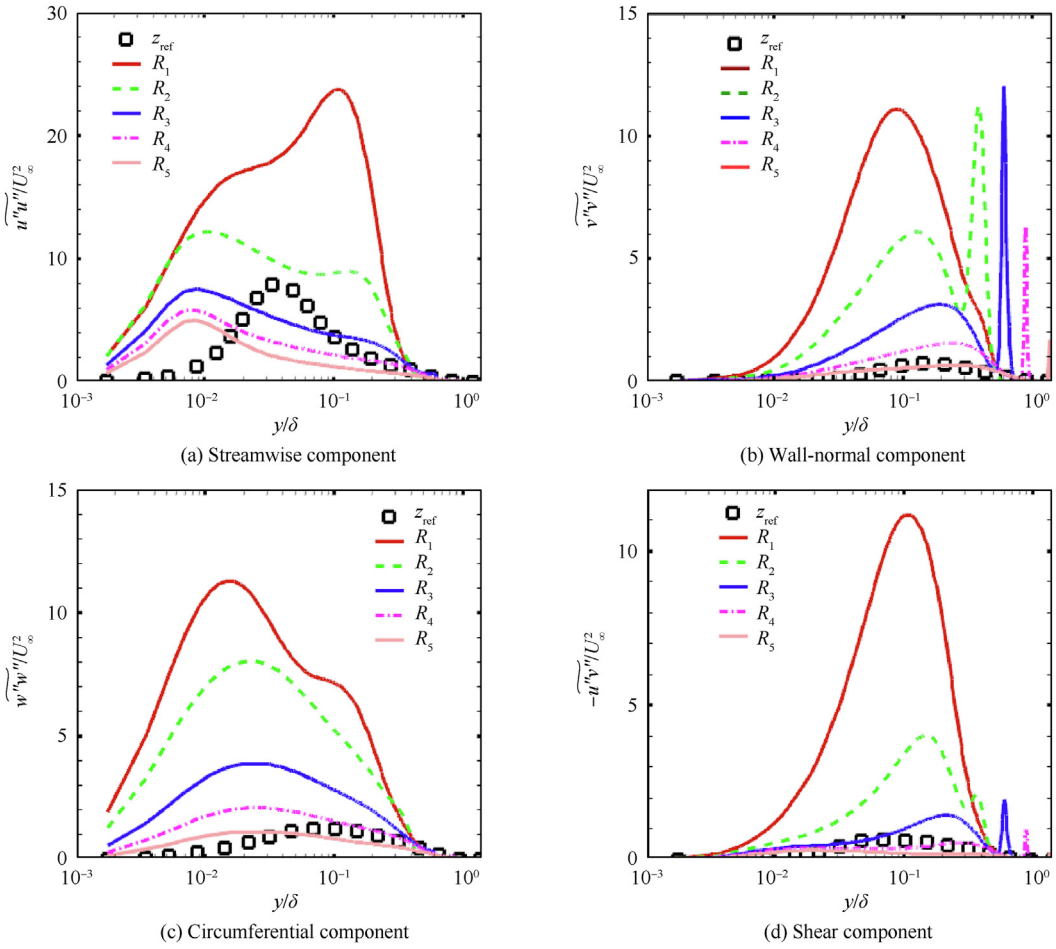

Fig. 12 Distribution of Reynolds stress tensor components at various locations.

Fig.12(d), where the profiles of the other three components quickly recover, and the differences between R_5 and z_{ref} are less significant.

Following the work of Lumley,[38] we show the Reynolds stress anisotropy invariant maps at various streamwise locations in Fig. 13 to further analyze the amplification of the Reynolds stress components; the second II_b and third III_b invariants of the anisotropy tensor b_{ij} are defined as

$$\begin{cases} b_{ij} = \dfrac{\widetilde{u_i'' u_j''}}{2u_k'' u_k''} - \frac{1}{3}\delta_{ij} \\ II_b = b_{ij}b_{ji} \\ III_b = b_{ij}b_{jk}b_{ki} \end{cases} \tag{6}$$

At z_{ref}, the anisotropy invariant map exhibits a typical characteristic of zero-pressure-gradient TBLs, as also observed in DNS studies by Sun et al.[39] In the near-wall region, two-component turbulence is attained and the anisotropy attains a maximum value in the buffer layer at $y/\delta \approx 0.029$ ($y^+ \approx 10$), which is in agreement with the numerical findings of Grilli et al.[8] and Pirozzoli et al.[40] As the wall-normal location moves outward, it is seen that the most turbulent state follows an axisymmetric expansion state, and the anisotropy of the flow in the outer region is further reduced, falling close to an isotropic state. At R_1, a substantial reduction of the anisotropy of the velocity fluctuations in the near-wall region occurs, as highlighted in Fig. 13(a). Turbulence in the immediate vicinity of the wall is characterized by a two-component axisymmetric state, and it closely resembles axisymmetric compression state in the inner part of the boundary layer $y/\delta < 0.025$. As y^+ is further increased, the anisotropy of the flow begins to increase and turbulence develops along the limit line of the axisymmetric expression state, attaining its maximum anisotropy at $y/\delta \approx 0.175$. Fig. 13(b)-Fig.13(d) shows a reversal tendency in the near-wall region at R_2–R_5, where the invariant trace is pulled toward the top right of the map, corresponding to a one-component turbulence state, suggesting that the anisotropy is significantly greater. This behavior is attributed to the regeneration of the elongated high-and low-speed streaks in the near-wall region.

Fig. 14 shows the distributions of the density-scaled turbulence kinetic energy k^+ as a function of wall-normal distance y^+ in local wall units at various streamwise locations. Upstream of the interaction, the TKE at z_{ref} attains a maximum value of $k^+ = 5.2$ at $y^+ = 15$, which is in close agreement with the computed values given by Patel et al.[41] for an incompressible TBL ($k^+ = 4.5$ at $y^+ = 15$) and by Pirozzoli et al.[27] for a spatially developing supersonic TBL ($k^+ = 5.25$ at $y^+ = 14.3$). As expected, the TKE at R_1 is greatly amplified, indicating turbulence amplification after passing

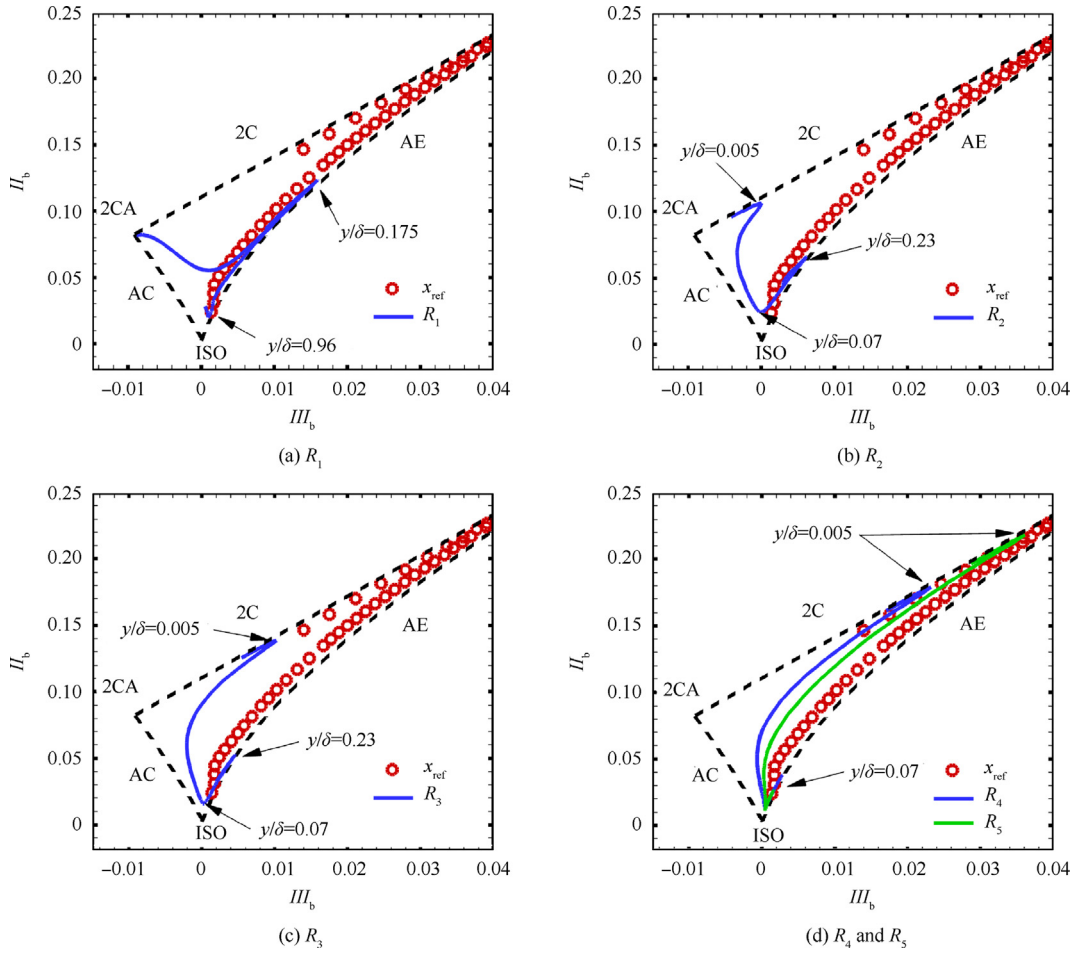

Fig. 13 Reynolds stress anisotropy invariant maps at various streamwise locations. ISO: isotropic; AC: axisymmetric compression; 2CA: two-component axisymmetric; AE: axisymmetric expansion; 2C: two components.

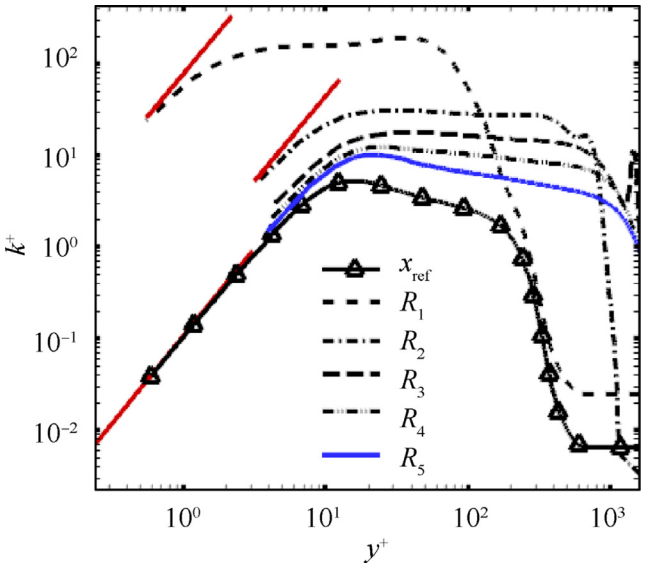

Fig. 14 Profiles of turbulent kinetic energy at various streamwise locations with the red solid lines being the correlation $k^+ = 0.2035y^{+2}$.

through the interaction. Moving downstream, the TKE decreases rapidly. It is also interesting to note that the TKE profile at z_{ref} obeys the near-wall asymptotic behavior, $k^+ \approx 0.2035y^{+2}$, but this asymptotic behavior is not satisfied in the near-wall region at R_1–R_5. Such a scenario shows essential differences from the findings of Pirozzoli et al.[27] and Tong et al.[20] in their DNS of supersonic STBLI flow. They argued that the asymptotic consistency was held at different constant values downstream of the interaction.

3.4. Mean skin friction decomposition

Useful information for understanding and predicting mean skin friction generation can be obtained using the Renard-Deck (RD) identity[42] to decompose the mean skin friction into physics-based contributions. We extend the method of Li et al.,[43] for the first time, to investigate the generation of the mean skin friction in hypersonic STBLI on a cone/flare. The mean skin friction decomposition in conical coordinates is expressed as

$$C_f = C_{f,V} + C_{f,T} + C_{f,G} + C_{f,R} \tag{7}$$

where $C_{f,V}$, $C_{f,T}$, $C_{f,G}$ and $C_{f,R}$ represent, respectively, the contributions of direct viscous dissipation, TKE production, the

Table 1 Fractal contributions to mean skin friction at various streamwise locations.

Location	$C_{f,\mathrm{V}}/C_f$ (%)	$C_{f,\mathrm{T}}/C_f$ (%)	$C_{f,\mathrm{G}}/C_f$ (%)	$C_{f,\mathrm{R}}/C_f$ (%)	Relative error (%)
z_{ref}	49.09	42.57	7.87	0.47	0
R_1	39.66	2994.16	−2945.62	4.98	−6.82
R_2	39.04	300.20	−240.81	0.42	−1.15
R_3	47.18	91.97	−39.02	0.14	0.27
R_4	49.66	54.65	−3.81	−0.11	0.39
R_5	49.11	41.93	9.38	−0.22	0.20

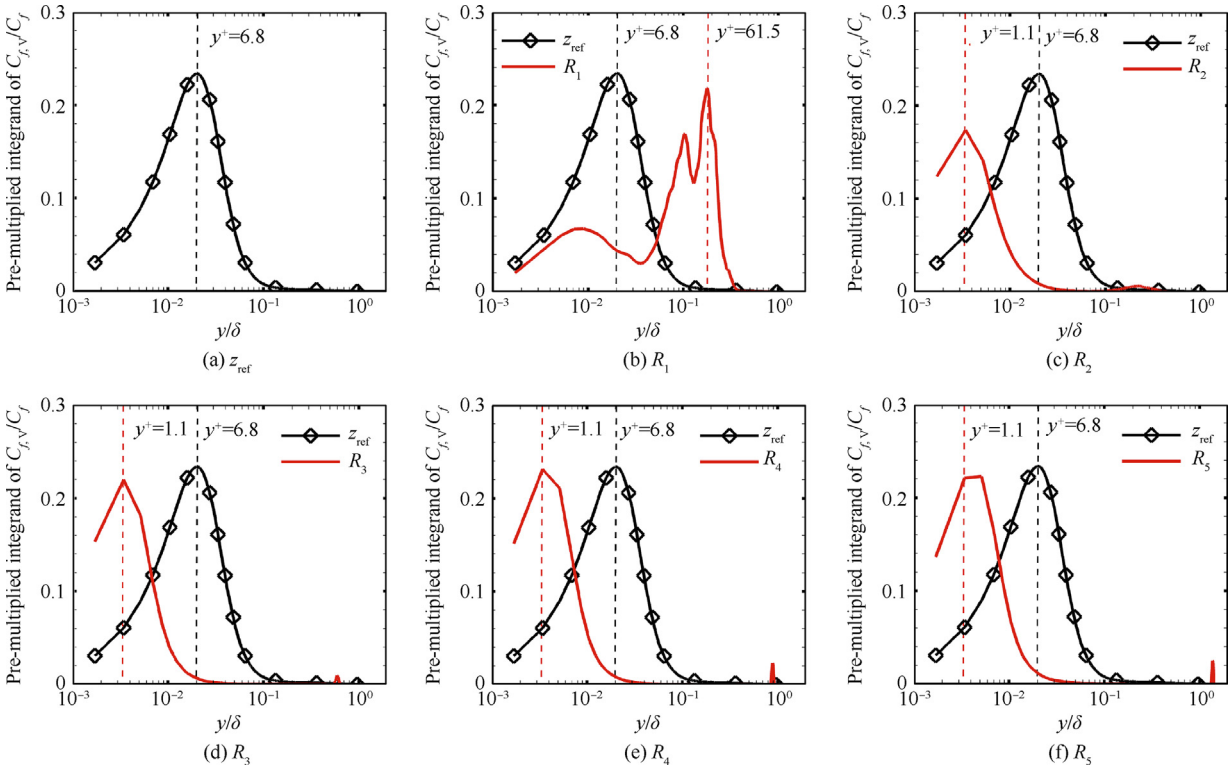

Fig. 15 Pre-multiplied integrands of $C_{f,\mathrm{V}}/C_f$ as a function of y/δ at various streamwise locations.

spatial growth of the flow, and the combined effect of transverse curvature and body divergence. Recalling the compressible RD identity proposed by Li et al.,[43] we highlight that the only difference in our decomposition is the transverse curvature and body divergence contribution $C_{f,\mathrm{R}}$, due to the body radius r. The explicit expressions for the four terms are given as

$$C_{f,\mathrm{V}} = \frac{2}{\rho_\infty U_\infty^3}\int_0^\infty \bar{\sigma}_{yx}\frac{\partial \widetilde{U}}{\partial y}\mathrm{d}y \tag{8}$$

$$C_{f,\mathrm{T}} = \frac{2}{\rho_\infty U_\infty^3}\int_0^\infty \bar{\rho}\left(-\widetilde{U''V''}\right)\frac{\partial \widetilde{U}}{\partial y}\mathrm{d}y \tag{9}$$

$$C_{f,\mathrm{G}} = \frac{2}{\rho_\infty U_\infty^3}\int_0^\infty \left(\widetilde{U}-U_\infty\right)\left[\bar{\rho}\left(\widetilde{U}\frac{\partial \widetilde{U}}{\partial x}+\widetilde{V}\frac{\partial \widetilde{V}}{\partial y}\right)+\frac{\partial}{\partial x}\left(\overline{\rho U''U''}-\bar{\sigma}_{xx}\right)+\frac{\partial \bar{p}}{\partial x}\right]\mathrm{d}y \tag{10}$$

$$C_{f,\mathrm{R}} = \frac{2}{\rho_\infty U_\infty^3}\int_0^\infty -\left(\widetilde{U}-U_\infty\right)\frac{\overline{\sigma_{rr}\sin\alpha+\sigma_{rz}\cos\alpha}}{r} + \left(\widetilde{U}-U_\infty\right)\frac{\bar{\rho}\widetilde{v''U''}}{r}\mathrm{d}y \tag{11}$$

Here, σ_{xx}, σ_{yx} and $\partial p/\partial x$ denote the normal viscous stress, the shear viscous stress and the pressure gradient in the x direction, respectively, and $\sigma_{\theta\theta}$, σ_{rr} and σ_{rz} are the components of the viscous stress in conical coordinates.

Considering that the mean skin friction is significantly increased downstream of the interaction, as previously shown in Fig. 3(b), we quantitatively compare the decomposed results at the five locations R_1–R_5 in the reattached boundary layer with those at the reference location z_{ref} in the upstream TBL to investigate the shock interaction on the skin friction generation. Table 1 lists the fractional contributions of the above four terms at different streamwise locations. The relative error, quantifying the deviation from the raw C_f, is defined as

$(C_{f,V} + C_{f,T} + C_{f,G} + C_{f,R} - C_f) / C_f$. As is apparent from Table 1, the relative errors are confined to within ±6.82%, demonstrating the high accuracy of this decomposition. In good agreement with the decomposition analysis by Fan et al.[44] of a spatially developing zero-pressure-gradient supersonic flat plate turbulent boundary layer, the mean skin friction at z_{ref} is dominated by $C_{f,V}$ and $C_{f,T}$, which contribute approximately 49.09% and 42.57%, respectively, to C_f, whereas the contributions of $C_{f,G}$ and $C_{f,R}$ are rather small and negligible. However, the decomposed results at R_1–R_4 show a completely different picture. Here, the positive contribution of $C_{f,T}$ plays the leading role, and rapidly decreases from 2994.16% at R_1 to 54.65% at R_4. Consistent with recent studies of reflected interactions by Zhang et al.[45] and Tong et al.[46], $C_{f,G}$ becomes negative and contributes significantly to C_f, in particular –2945.62% at R_1 and –240.81% at R_2. It is suggested that the small positive C_f downstream of the interaction is mainly produced by the very large positive $C_{f,T}$ and the very large negative $C_{f,G}$. At R_5, the negative $C_{f,G}$ becomes positive and the contribution of $C_{f,V}$ becomes dominant again, showing close similarities with the decomposition in the upstream TBL. It is also emphasized that the influence of the direct shock interaction on the contribution of $C_{f,R}$ can be negligible, where $C_{f,R}/C_f$ is very small in the downstream region.

To obtain a more intuitive understanding, we also show profiles of the pre-multiplied integrands of the significant components in the wall-normal direction at various streamwise locations, where the area below the curve is in proportion to the ratio $C_{f,V}/C_f$, $C_{f,T}/C_f$ or $C_{f,G}/C_f$. The results at z_{ref} are also included for reference.

In Fig. 15(a), the pre-multiplied integrand of $C_{f,V}/C_f$ at z_{ref} peaks at $y/\delta = 0.02$ ($y^+ = 6.8$) and the contribution of $C_{f,V}$ mainly comes from the inner region $y/\delta < 0.1$. At R_1, it is seen in Fig. 15(b) that the profile shape is different, with the peak located at $y^+ = 61.5$ and most of $C_{f,V}$ is generated in the region $0.04 < y/\delta < 0.4$, indicative of the great importance of the outer region just after passing through the interaction. At R_2–R_5 (see Fig. 15(c)-Fig.15(f)), the profiles have recovered and shown the similarities with that of the upstream TBL, but the peak reappears in the very-near-wall region, being approximately fixed at a wall-normal location of $y/\delta = 0.003$ ($y^+ = 1.1$), which is independent of the relaxation process.

Regarding the pre-multiplied integrand of $C_{f,T}/C_f$, as displayed in Fig. 16, a similar evolution process in the reattachment region is observed. As shown in Fig. 16(a), the peak at z_{ref} is located in the near-wall region at $y/\delta = 0.043$ ($y^+ = 14.8$), while a secondary peak is identified in the logarithmic region at $y/\delta = 0.31$ ($y^+ = 104$). Such double-peak behavior is very similar to that seen in the decomposition analysis of Fan et al.[44] in zero-pressure-gradientflat plate turbulent boundary layers; they suggested that the secondary peak could be ascribed to the generation of large-scale energy-containing motions in the logarithmic and outer regions. Additionally, the computed secondary peak location y^+_{2nd} in the present study is consistent with the linear relationship $y^+_{2nd} = 0.43Re_\tau - 10.11$ proposed by Fan et al.[44] In Fig. 16(b)-Fig. 16(c), it is seen that the profiles at R_1 and R_2 are characterized by a single outer peak, appearing at $y/\delta = 0.16$ and 0.20, respectively, and $C_{f,T}$ is mainly generated in the region $y/\delta = 0.043$–0.31. This is mainly related to the outer large-scale structures downstream

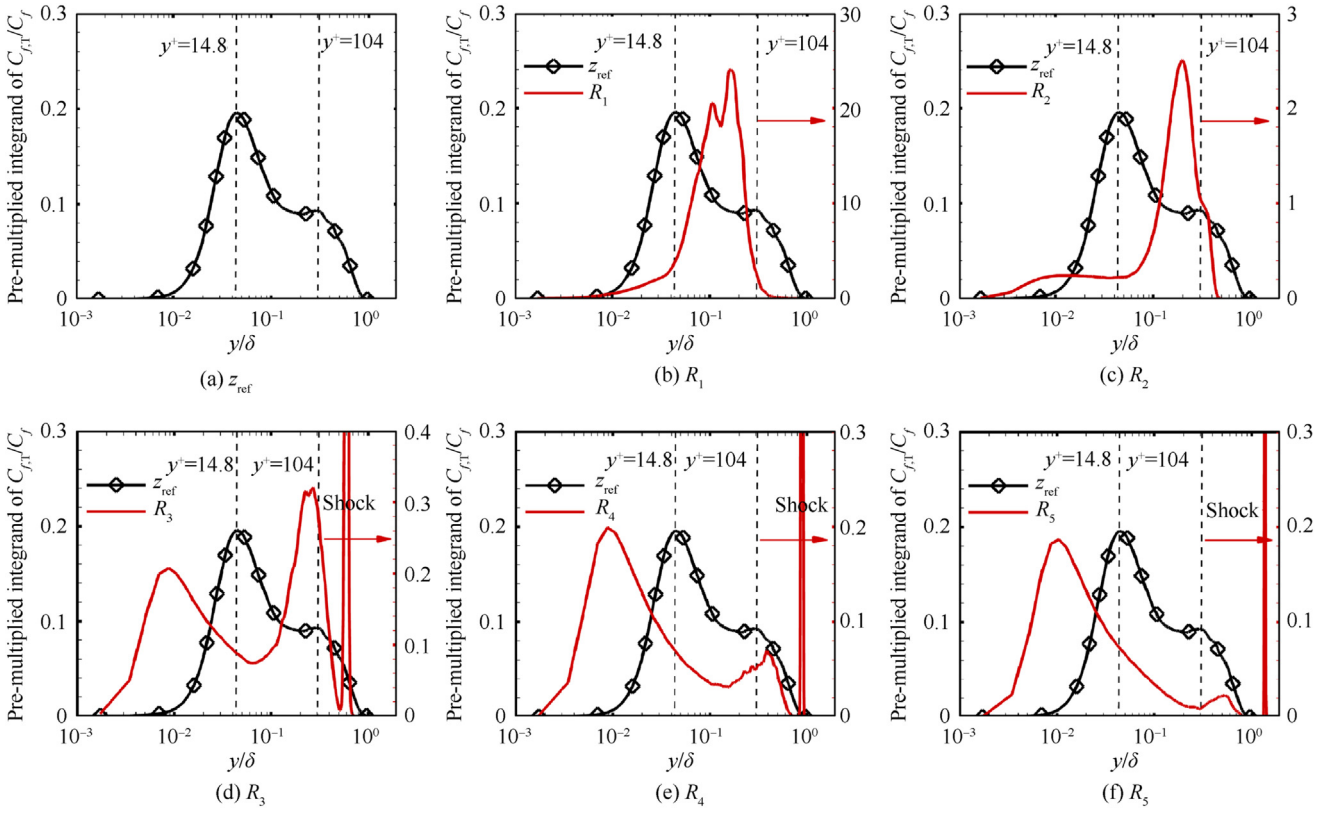

Fig. 16 Pre-multiplied integrands of $C_{f,T}/C_f$ as a function of y/δ at various streamwise locations.

of the interaction and will be quantitatively analyzed in the following. Going from R_3 to R_5, as the reattached boundary layer has developed further downstream, the profiles shown in Fig. 16(d)-Fig. 16(f) relax toward the upstream double-peaked distribution at z_{ref}. Note that the strong spikes in the figures are caused by the shock wave located above the boundary layer. Clearly, the outer peak decreases rapidly, with its location moving slightly outward, whereas the inner peak reoccurs at $y/\delta < 0.01$ and significantly increases. It is seen from Fig. 16(f) that the inner peak is close to that at z_{ref}, with its location being lower, while the outer peak is much smaller than the upstream value, suggesting that the relaxation process is incomplete inside the entire boundary layer.

Similar to the analysis of Duan et al.,[47] we further break down the $C_{f,\mathrm{T}}$ contribution into various circumferential length scales. At a given y location, the cospectra of the Reynolds shear stress in Eq. (9) are defined as.

$$\Phi_{UV}(k_s, y) = c\langle \mathrm{Re}\left[\widehat{U}(k_s, y)\widehat{V}^*(k_s, y)\right]\rangle \tag{12}$$

where $\widehat{U}(k_s, y)$ and $\widehat{V}(k_s, y)$ are the Fourier transform of u and v, respectively, in the circumferential direction, and k_s is the circumferential wavenumber. The angle brackets $< >$, superscript asterisk $*$ and Re[ ] denote the ensemble averaging, complex conjugate and real part of a complex number, respectively. The constant c is calculated as satisfying.

$$\widetilde{UV} = \int_0^\infty \Phi_{UV}(k_s)\mathrm{d}k_s \tag{13}$$

The fractal contribution $C_{f,\mathrm{T}}/C_f$ can be explicitly expressed as

$$\frac{C_{f,\mathrm{T}}}{C_f} = \int_{-\infty}^{\infty}\int_{-\infty}^{\infty} \frac{k_s y \Phi_{\mathrm{RD}}}{C_f}\mathrm{d}(\ln k_s)\mathrm{d}(\ln y) \tag{14}$$

where Φ_{RD} represents the weighted contribution of the Reynolds shear stress to C_f, and is given by.

$$\Phi_{\mathrm{RD}} = \frac{2}{\rho_\infty U_\infty^3}\bar{\rho}\frac{\partial \widetilde{U}}{\partial y}\Phi_{UV} \tag{15}$$

Correspondingly, the integrand function $k_s y\Phi_{\mathrm{RD}}/C_f$ in the λ-y plane on logarithmic scales represents the contribution of a given circumferential wavelength λ at a given location y to C_f.

Fig. 17 shows the integrand function $k_s y\Phi_{\mathrm{RD}}/C_f$ at three streamwise locations, showing variation with both inner scales (λ^+ and y^+). The spectra are normalized by the maximum value. At z_{ref} (see Fig. 17(a)), the most significant contribution appears at $y^+ = 15.4$ and $\lambda^+ = 87.1$. In Fig. 17(b), we observe that the peak location moves outward and the peak wavelength becomes much larger, so that $y^+ = 54.9$ and $\lambda^+ = 177.8$ at R_1. Such behavior is consistent with the above analysis of Fig. 16(a)-Fig. 16(b). At R_5, Fig. 17(c) shows the strongest contribution at $y^+ = 3.3$ and $\lambda^+ = 25.9$, suggesting that the $C_{f,\mathrm{T}}$ contribution is mainly associated with the small-scale fluctuations in the very-near-wall region. It is seen that the peak wavelength at R_5 is still much smaller than that at z_{ref}, also indicating that the recovery process is incomplete. Recalling the analysis of the pre-multiplied integrands in Fig. 16, we see that the generation of $C_{f,\mathrm{T}}$ in the reattached boundary layer is characterized by the transformation from large-scale turbu-

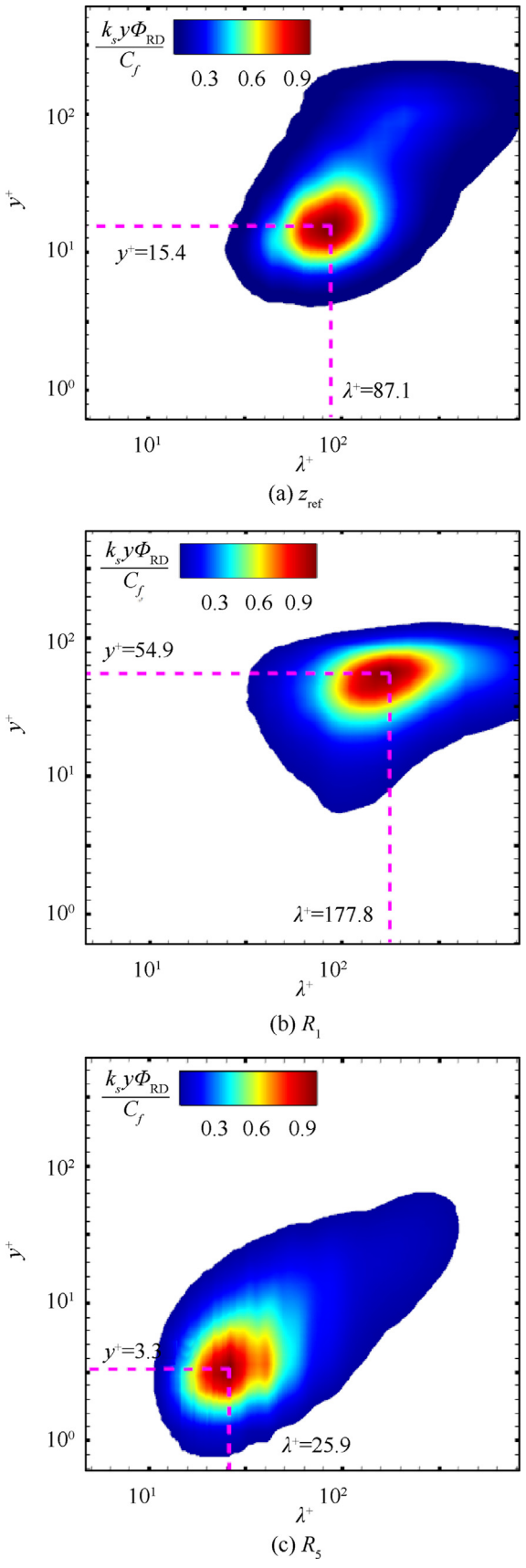

Fig. 17 Local $C_{f,\mathrm{T}}$ contribution at three streamwise locations.

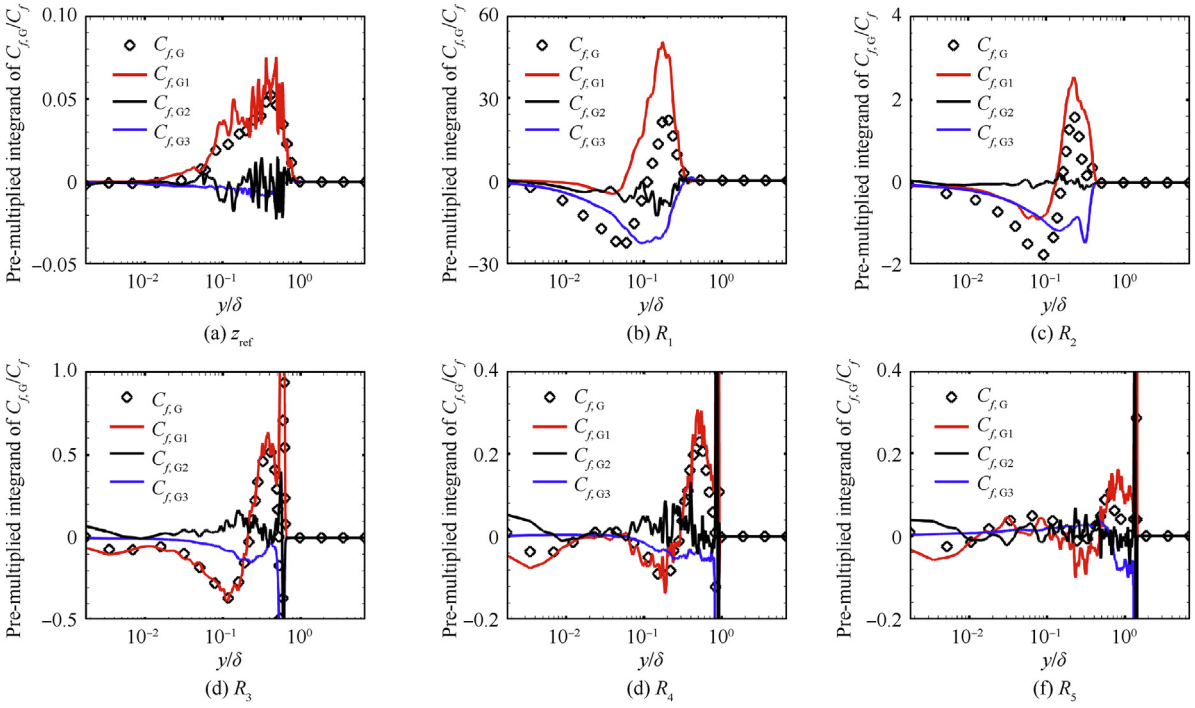

Fig. 18 Pre-multiplied integrands of $C_{f,G}/C_f$ as a function of y/δ at various streamwise locations.

lence in the outer region to small-scale turbulence in the near-wall region.

According to Eq. (8), the contribution $C_{f,G}$ can be decomposed as.

$$C_{f,G} = C_{f,G1} + C_{f,G2} + C_{f,G3} \tag{16}$$

where

$$C_{f,G1} = \frac{2}{\rho_\infty U_\infty^3}\int_0^\infty \left(\widetilde{U} - U_\infty\right)\left[\bar{\rho}\left(\widetilde{U}\frac{\partial \widetilde{U}}{\partial x} + \widetilde{V}\frac{\partial \widetilde{V}}{\partial y}\right)\right]\mathrm{d}y \tag{17}$$

$$C_{f,G2} = \frac{2}{\rho_\infty U_\infty^3}\int_0^\infty \frac{\partial}{\partial x}\left(\rho\widetilde{U''U''} - \bar{\sigma}_{xx}\right)\mathrm{d}y \tag{18}$$

$$C_{f,G3} = \frac{2}{\rho_\infty U_\infty^3}\int_0^\infty \frac{\partial \bar{p}}{\partial x}\mathrm{d}y \tag{19}$$

Here, $C_{f,G1}$, $C_{f,G2}$ and $C_{f,G3}$ denote the convective term, the streamwise-heterogeneity term and the pressure-gradient term, respectively. Therefore, the pre-multiplied integrand of $C_{f,G}/C_f$ consists of three corresponding parts: $C_{f,G1}/C_f$, $C_{f,G2}/C_f$ and $C_{f,G3}/C_f$, as show in Fig. 18. At R_1, the positive $C_{f,G}$ (see Fig. 18(a)), confined to the outer region, is mainly related to the positive $C_{f,G1}$, whereas the magnitudes of the other two terms are rather small and can be neglected. However, the pre-multiplied integrands at R_1 and R_2 reveal a different scenario in Fig. 18(b)-Fig. 18(c). The curves of $C_{f,G}$ exhibit a sign switching, being negative in the near-wall region and positive in the outer region. Such behavior is the combined result of the very large positive $C_{f,G1}$ and the very large negative $C_{f,G3}$, consistent with the recent decomposition analysis of Fan et al.[48] on adverse pressure gradient turbulent boundary layers developing on flat plates and airfoils. As seen from Fig. 18(d)-Fig. 18(f), $C_{f,G3}$ rapidly decreases due to the reduction of the pressure gradient in the downstream region, and the contribution $C_{f,G1}$ is again dominant over most of the boundary layer.

4. Conclusions

A DNS of a hypersonic sharp cone/flare configuration has been performed. The numerical study has focused on the fundamental mechanisms dictating the hypersonic interaction, including mean and instantaneous properties, turbulence evolution and the decomposition of mean skin friction.

(1) The simulation shows that the mean flow is separated and a substantial unsteadiness of the moving separation bubble is observed near the corner. The Reynolds analogy and QP85 scaling are not satisfied in the interaction zone. Downstream of the interaction, RAF is about 1.06–1.27, very close to the upstream value, whereas QP85 is maintained at a nearly constant value of 0.5, half of the upstream value.

(2) The study shows that the turbulence is strongly amplified, especially for the wall-normal component of the Reynolds stresses. The reduced turbulence anisotropy slowly increases as the reattached boundary layer relaxes downstream. The downstream TKE does not obey follow near-wall asymptotic behavior, which is different from the findings in previously studied supersonic interactions.

(3) The mean skin friction decomposition exhibits similarities with the reflected interaction, where the generation in the downstream region is dominated by the positive contribution related to TKE production and the nega-

tive contribution associated with spatial growth of the flow. The positive contribution is mainly linked to the counterbalance between the outer large-scale and inner small-scale turbulence. The convective term and the pressure gradient term contribute most to the negative spatial growth contribution. The combined effect of transverse curvature and body divergence on the generation is negligible.

Declaration of Competing Interest

The authors declare that they have no known competing financial interests or personal relationships that could have appeared to influence the work reported in this paper.

Acknowledgements

This study was co-supported by the National Natural Science Foundation of China (Nos. 11972356 and 91852203) and the National Key Research and Development Program of China (No. 2019YFA0405300).

References

1. Green JE. Interactions between shock waves and turbulent boundary layers. *Prog Aerosp Sci* 1970;**11**:235–340.
2. Dolling DS. Fifty years of shock-wave/boundary-layer interaction research: What next? *AIAA J* 2001;**39**(8):1517–31.
3. Gaitonde DV. Progress in shock wave/boundary layer interactions. *Prog Aerosp Sci* 2015;**72**:80–99.
4. Clemens NT, Narayanaswamy V. Low-frequency unsteadiness of shock wave/turbulent boundary layer interactions. *Annu Rev Fluid Mech* 2014;**46**(1):469–92.
5. Pasquariello V, Hickel S, Adams NA. Unsteady effects of strong shock-wave/boundary-layer interaction at high Reynolds number. *J Fluid Mech* 2017;**823**:617–57.
6. Dupont P, Haddad C, Debiève JF. Space and time organization in a shock-induced separated boundary layer. *J Fluid Mech* 2006;**559**:255–77.
7. Grilli M, Schmid PJ, Hickel S, Adams NA. Analysis of unsteady behaviour in shockwave turbulent boundary layer interaction. *J Fluid Mech* 2012;**700**:16–28.
8. Grilli M, Hickel S, Adams NA. Large-eddy simulation of a supersonic turbulent boundary layer over a compression-expansion ramp. *Int J Heat Fluid Flow* 2013;**42**:79–93.
9. Fang J, Zheltovodov AA, Yao Y, et al. On the turbulence amplification in shock-wave/turbulent boundary layer interaction. *J Fluid Mech* 2020;**897**. https://doi.org/10.1017/jfm.2020.350.
10. Priebe S, Tu JH, Rowley CW, Martín MP. Low-frequency dynamics in a shock-induced separated flow. *J Fluid Mech* 2016;**807**:441–77.
11. Zhuang Yi, Tan H-J, Li X, Sheng F-J, Zhang Y-C. Letter: Görtler-like vortices in an impinging shock wave/turbulent boundary layer interaction flow. *Phys Fluids* 2018;**30**(6):061702.
12. Mikulla V, Horstman CC. Turbulence measurements in hypersonic shock-wave boundary-layer interaction flows. *AIAA J* 1976;**14**(5):568–75.
13. Bookey P, Wyckham C, Smits A, et al. New experimental data of STBLI at DNS/LES accessible Reynolds numbers. *43rd AIAA aerospace sciences meeting and exhibit*; 2005 Jan 10-13; Reno, Nevada. Reston: AIAA; 2005.
14. Schrijer FFJ, Scarano F, van Oudheusden BW. Application of PIV in a Mach 7 double-ramp flow. *Exp Fluids* 2006;**41**(2):353–63.
15. Brooks J, Gupta A, Marineau EC, et al. Mach 10 PIV flow field measurements of a turbulent boundary layer and shock turbulent boundary layer interaction. *33rd AIAA aerodynamic measurement technology and ground testing conference*; 2017 Jun 5-9; Denver, Colorado. Reston: AIAA; 2017.
16. Schreyer A-M, Sahoo D, Williams OJH, Smits AJ. Experimental investigation of two hypersonic shock/turbulent boundary-layer interactions. *AIAA J* 2018;**56**(12):4830–44.
17. Priebe S, Martín MP. Turbulence in a hypersonic compression ramp flow. *Phys Rev Fluids* 2021;**6**(3):034601.
18. Running CL, Juliano TJ, Jewell JS, et al. Hypersonic shock-wave/boundary-layer interactions on a cone/flare. *Exp Therm Fluid Sci* 2019;**109**:109911.
19. Tong F, Li X, Duan Y, et al. Direct numerical simulation of supersonic turbulent boundary layer subjected to a curved compression ramp. *Phys Fluids* 2017;**29**(12):125101.
20. Tong F, Sun D, Li X. Direct numerical simulation of impinging shock wave and turbulent boundary layer interaction over a wavy-wall. *Chin J Aeronaut* 2021;**34**(5):350–63.
21. Martín MP, Taylor EM, Wu M, Weirs VG. A bandwidth-optimized WENO scheme for the effective direct numerical simulation of compressible turbulence. *J Comput Phys* 2006;**220**(1):270–89.
22. Wu M, Martin MP. Direct numerical simulation of supersonic turbulent boundary layer over a compression ramp. *AIAA J* 2007;**45**(4):879–89.
23. Gottlieb S, Shu C-W. Total variation diminishing Runge-Kutta schemes. *Math Comp* 1998;**67**(221):73–85.
24. Sivasubramanian J, Fasel HF. Direct numerical simulation of transition in a sharp cone boundary layer at Mach 6: fundamental breakdown. *J Fluid Mech* 2015;**768**:175–218.
25. Pirozzoli S, Grasso F, Gatski TB. Direct numerical simulation and analysis of a spatially evolving supersonic turbulent boundary layer at M = 2.25. *Phys Fluids* 2004;**16**(3):530–45.
26. Li X, Fu D, Ma Y. Direct numerical simulation of hypersonic boundary layer transition over a blunt cone with a small angle of attack. *Phys Fluids* 2010;**22**(2):025105.
27. Pirozzoli S, Grasso F. Direct numerical simulation of impinging shock wave/turbulent boundary layer interaction at M = 2.25. *Phys Fluids* 2006;**18**(6):065113.
28. Tong F, Yu C, Tang Z, et al. Numerical studies of shock wave interactions with a supersonic turbulent boundary layer in compression corner: turning angle effects. *Comput Fluids* 2017;**149**:56–69.
29. Pirozzoli S, Bernardini M, Grasso F. Characterization of coherent vortical structures in a supersonic turbulent boundary layer. *J Fluid Mech* 2008;**613**:205–31.
30. Subbareddy P, Candler G. DNS of transition to turbulence in a hypersonic boundary layer. *41st AIAA fluid dynamics conference and exhibit*; 2011 Jun 27-30; Honolulu, Hawaii. Reston: AIAA; 2011.
31. Priebe S, Martín MP. Low-frequency unsteadiness in shock wave-turbulent boundary layer interaction. *J Fluid Mech* 2012;**699**:1–49.
32. Roy CJ, Blottner FG. Review and assessment of turbulence models for hypersonic flows. *Prog Aerosp Sci* 2006;**42**(7-8):469–530.
33. Back LH, Cuffel RF. Changes in heat transfer from turbulent boundary layers interacting with shock waves and expansion waves. *AIAA J* 1970;**8**(10):1871–3.
34. Murray N, Hillier R, Williams S. Experimental investigation of axisymmetric hypersonic shock-wave/turbulent-boundary-layer interactions. *J Fluid Mech* 2013;**714**:152–89.
35. Walz A. *Boundary layers of flow and temperature*. Cambridge: MIT Press; 1969.
36. Volpiani PS, Bernardini M, Larsson J. Effects of a nonadiabatic wall on supersonic shock/boundary-layer interactions. *Phys Rev Fluids* 2018;**3**(8):083401.
37. Loginov M, Adams NA, Zheltovodov AA. Large-eddy simulation of shock-wave/turbulent- boundary layer interaction. *J Fluid Mech* 2006;**565**:133–69.

38. Lumley JL. Computational modeling of turbulent flows*. *Adv Appl Mech* 1979;**18**:123–76.
39. Sun M, Sandham ND, Hu Z. Turbulence structures and statistics of a supersonic turbulent boundary layer subjected to concave surface curvature. *J. Fluid Mech*. 2019;**865**:60–99.
40. Pirozzoli S, Bernardini M, Grasso F. Direct numerical simulation of transonic shock/boundary layer interaction under conditions of incipient separation. *J Fluid Mech* 2010;**657**:361–93.
41. Patel VC, Rodi W, Scheuerer G. Turbulence models for near-wall and low Reynolds number flows - A review. *AIAA J* 1985;**23**(9):1308–19.
42. Renard N, Deck S. A theoretical decomposition of mean skin friction generation into physical phenomena across the boundary layer. *J Fluid Mech* 2016;**790**:339–67.
43. Li W, Fan Y, Modesti D, et al. Decomposition of the Mean skin-friction drag in compressible turbulent channel flows. *J Fluid Mech* 2019;**875**:101–23.
44. Fan YT, Li WP, Pirozzoli S. Decomposition of the mean friction drag in zero-pressure-gradient turbulent boundary layers. *Phys Fluids* 2019;**31**(8):086105.
45. Zhang Z, Tong F, Duan J, et al. Direct numerical simulation of supersonic turbulent expansion corner with shock impingement. *Phys Fluids* 2021;**33**(10):105104.
46. Tong F, Duan J, Li X. Characteristics of reattached boundary layer in shock wave and turbulent boundary layer interaction. *Chin J Aeronaut* 2022;**35**(6):172–85.
47. Duan Y, Zhong Q, Wang G, et al. Contributions of different scales of turbulent motions to the Mean wall-shear stress in open channel flows at low-to-moderate Reynolds numbers. *J Fluid Mech* 2021;**918**:A40.
48. Fan Y, Li W, Atzori M, et al. Decomposition of the mean friction drag in adverse-pressure-gradient turbulent boundary layers. *Phys Rev Fluids* 2020;**5**(11):114608.